

RadMamba: Efficient Human Activity Recognition through Radar-based Micro-Doppler-Oriented Mamba State-Space Model

Yizhuo Wu[✉], *Student Member, IEEE*, Francesco Fioranelli[✉], *Senior Member, IEEE*
Chang Gao[✉], *Member, IEEE*,

Abstract—Radar-based Human Activity Recognition (HAR) has emerged as a promising alternative to conventional monitoring approaches, such as wearable devices and camera-based systems, due to its unique privacy preservation and robustness advantages. However, existing solutions based on convolutional and recurrent neural networks, although effective, are computationally demanding during deployment. This limits their applicability in scenarios with constrained resources or those requiring multiple sensors. Advanced architectures, such as Vision Transformer (ViT) and State Space Model (SSM) architectures, offer improved modeling capabilities and have made efforts toward lightweight designs. However, their computational complexity remains relatively high. To leverage the strengths of transformer architectures while simultaneously enhancing accuracy and reducing computational complexity, this paper introduces *RadMamba*, a parameter-efficient, radar micro-Doppler-oriented Mamba SSM specifically tailored for radar-based HAR. Across three diverse datasets, RadMamba matches the top-performing previous model's 99.8% classification accuracy on Dataset DIAT with only 1/400 of its parameters and equals the leading models' 92.0% accuracy on Dataset CI4R with merely 1/10 of their parameters. In scenarios with continuous sequences of actions evaluated on Dataset UoG2020, RadMamba surpasses other models with significantly higher parameter counts by at least 3%, achieving this with only 6.7k parameters. Our code is available at: <https://github.com/lab-emi/AIRHAR>.

Index Terms—Human activity recognition, Mamba state-space model, Frequency Modulated Continuous Wave (FMCW) radar, micro-Doppler signatures, deep learning, parameter-efficient networks, continuous monitoring, radar signal processing

I. INTRODUCTION

HUMAN Activity Recognition (HAR) technologies have become increasingly critical in modern society, finding essential applications in healthcare, elderly care, smart homes, and security. Traditional HAR methods predominantly rely on wearable sensors or camera-based systems. While wearable devices offer precise monitoring, they often compromise user comfort and face challenges related to battery life and user compliance. Camera-based solutions, although versatile, introduce significant privacy concerns and are susceptible to performance degradation under challenging environmental conditions. Consequently, Radar-based Human Activity Recognition (RadHAR) systems have emerged as a compelling alternative due to their inherent advantages, including user pri-

vacuity preservation, robustness to light conditions, non-intrusive and through-wall sensing capabilities [1], [2].

The field of radar-based HAR has evolved considerably from initial works focusing on simple scenarios with clearly defined activities [3], [4] toward more complex and realistic settings, including continuous activity monitoring [5], [6], multi-modal and distributed sensing [7], [8], and advanced classification techniques based on machine learning and deep learning methods. Early solutions predominantly relied on conventional machine learning algorithms, such as Support Vector Machines (SVMs) and k-Nearest Neighbors (kNN), utilizing handcrafted features like micro-Doppler centroid, bandwidth, and statistical measures [4]–[6]. Although these traditional techniques demonstrated acceptable performance in constrained scenarios, they encountered challenges related to scalability, complexity in feature engineering, and generalization to realistic continuous environments.

The advent of deep learning techniques, particularly convolutional neural networks (CNNs) [9], [10], recurrent neural networks (RNNs) [7], [11], and hybrid CNN-RNN models [12]–[14], revolutionized radar-based HAR by enabling automatic extraction and representation of complex spatial-temporal features directly from radar data. However, despite their accuracy, CNN and hybrid models typically suffer from high computational complexity and latency, limiting their suitability for real-time deployment, especially in resource-constrained edge scenarios.

Recently, advanced transformer-based architectures such as ViT and SSM have demonstrated significant improvements in feature modeling capabilities and explored lightweight designs across various domains [15]–[20]. Nevertheless, their computational complexity remains high, making it challenging to balance the number of parameters and the number of floating-point operations per inference (#FLOP/Inf.). For instance, the FML-ViT model with only 169M #FLOP/Inf. requires 2.7M parameters [16], while model LW-ViT with 769k parameters demands significantly higher #FLOP [21]. Compared to ultra-lightweight object detection models optimized for edge devices, such as YOLO-Fastest with 350k parameters, and 252M #FLOP/Inf, the direct application of these advanced architectures to radar-based HAR tasks remains costly due to their high computational overhead. This limitation is particularly critical for applications with limited resources, such as gesture recognition in assistive technologies on mobile or embedded devices [22]. Additionally, applications like smart

Yizhuo Wu, Francesco Fioranelli, and Chang Gao are with the Department of Microelectronics, Delft University of Technology, The Netherlands.

*Corresponding author: Chang Gao (chang.gao@tudelft.nl)

home monitoring, which often involve multiple sensors deployed across a home, would greatly benefit from lightweight and energy-efficient algorithms [8].

To overcome these limitations and leverage the modeling strengths of state-space architectures while ensuring computational efficiency in radar-based HAR, we introduce a novel SSM Mamba-based architecture named **RadMamba**. In summary, the main contributions of this work are as follows:

- We propose RadMamba, a parameter-efficient radar-based HAR architecture incorporating Channel Fusion and Downsampling, Doppler-aligned segmentation, and convolutional token projections, specifically tailored to address the unique characteristics of micro-Doppler radar signatures.
- RadMamba achieves state-of-the-art classification accuracy on multiple radar-based HAR datasets: it matches the best accuracy of existing heavyweight models on non-continuous datasets (99.8% accuracy on Dataset DIAT and 91.2% accuracy on Dataset CI4R), and surpasses existing models by at least 3% on scenarios with continuous sequences of activities (89.3% accuracy on Dataset UoG2020), all while significantly reducing the number of parameters. Moreover, its computational complexity is the lowest compared to previous models validated on Dataset CI4R and Dataset UoG2020.
- We perform a comprehensive ablation study demonstrating the critical role and synergy of each proposed architectural component, showing that the combination of micro-Doppler-aligned segmentation, adaptive downsampling, and convolutional projections is essential for optimal performance.
- We provide an open-source PyTorch framework, RadHAR, facilitating rapid prototyping and evaluation of micro-Doppler-based HAR methods, promoting reproducibility and future research.

II. RELATED WORKS

A. Conventional machine learning method

These methods involved extracting domain-specific features from radar signals, followed by classification using algorithms like kNN and SVM. For instance, Erol et al. [5] used kNN to analyze power burst curves in spectrograms for fall detection, distinguishing fall from non-fall events. Li et al. [6] applied SVMs to micro-Doppler features such as Doppler centroid, bandwidth, and Singular Value Decomposition (SVD) components, while Ding et al. [23] extracted 28 features of four types: dynamic Doppler frequency, range change, energy change and dispersion of range and Doppler from dynamic range-Doppler trajectories for subspace kNN classification. Although effective in controlled environments, these approaches struggled to generalize across diverse conditions and activities due to their dependence on hand-crafted features, often leading to overfitting and poor scalability for continuous tasks [1], [2].

B. CNN-based method

The shift to deep learning marked a turning point for RadHAR, with Convolutional Neural Networks (CNNs) lead-

ing the charge. Unlike traditional methods, CNNs automatically learn spatial hierarchies from radar representations like spectrograms and range-Doppler maps. Kang et al. [24] employed CNNs in a two-step process for segmenting and classifying activity sequences, achieving over 97% segmentation accuracy and 95% classification accuracy with 60 GHz millimeter-wave radar data. Yu et al. [10] introduced a ‘Dual-View CNN’ operating on orthogonal projections of voxelized point clouds, reaching 97.61% accuracy. However, CNNs applied solely on micro-Doppler maps simply treated as images, lacks inherent temporal modeling, a critical limitation for continuous activity recognition.

C. RNN-based method

To address temporal dynamics in human activities, researchers incorporated Recurrent Neural Networks (RNNs), particularly Long Short-Term Memory (LSTM) [25] and Gated Recurrent Unit (GRU) [26] networks, specifically designed for sequential data processing. Shrestha et al. [27] demonstrated the superiority of bidirectional LSTM networks over traditional SVMs and standard LSTMs in continuous activity recognition. Werthen-Brabants et al. [11] proposed an innovative split Bidirectional (Bi)-RNN architecture for real-time fall alerts, using separate forward & backward RNN components for immediate, refined predictions.

D. Hybrid CNN-RNN-based method

Recognizing the complementary strengths of CNNs and RNNs, hybrid architectures emerged as a dominant paradigm. These models typically combine CNN-based spatial feature extraction with RNN-based temporal modeling. Kurtoglu et al. [12] implemented a sophisticated multi-modal approach, utilizing 3D CNNs with Bi-LSTM layers for range-Doppler maps and 2D/1D CNNs with Bi-LSTM for spectrograms and envelopes, achieving 93.3% accuracy for continuous activities mixed with American Sign Language [28]. Zhu et al. [13] integrated CNN-extracted features with LSTM-based temporal modeling, achieving 98.65% accuracy on a non-continuous Doppler radar human activity recognition task with 7 classes.

For distributed radar systems, hybrid models achieve an accuracy of 87.1% in continuous activity recognition tasks with only 71 k parameters [14]. Compared to CNN-based models in non-continuous tasks that utilize 135 M parameters [29] and RNN-based models in continuous tasks that utilize 189 M parameters [27] to achieve their best classification accuracy, hybrid models are more lightweight. However, the Floating-point Operation (FLOP) required by the hybrid model [14] is evaluated to be at least 1 G. The arithmetic intensity of CNNs, especially for multi-channel signals, drives their computational complexity.

E. Transformer and SSM-based method

Recently, researchers have explored transformer-based architectures and SSM in RadHAR. ViT-based methods [16] achieved 92% accuracy with 2.7 M parameters, while [21] reached 92.1% with 769 k parameters on non-continuous

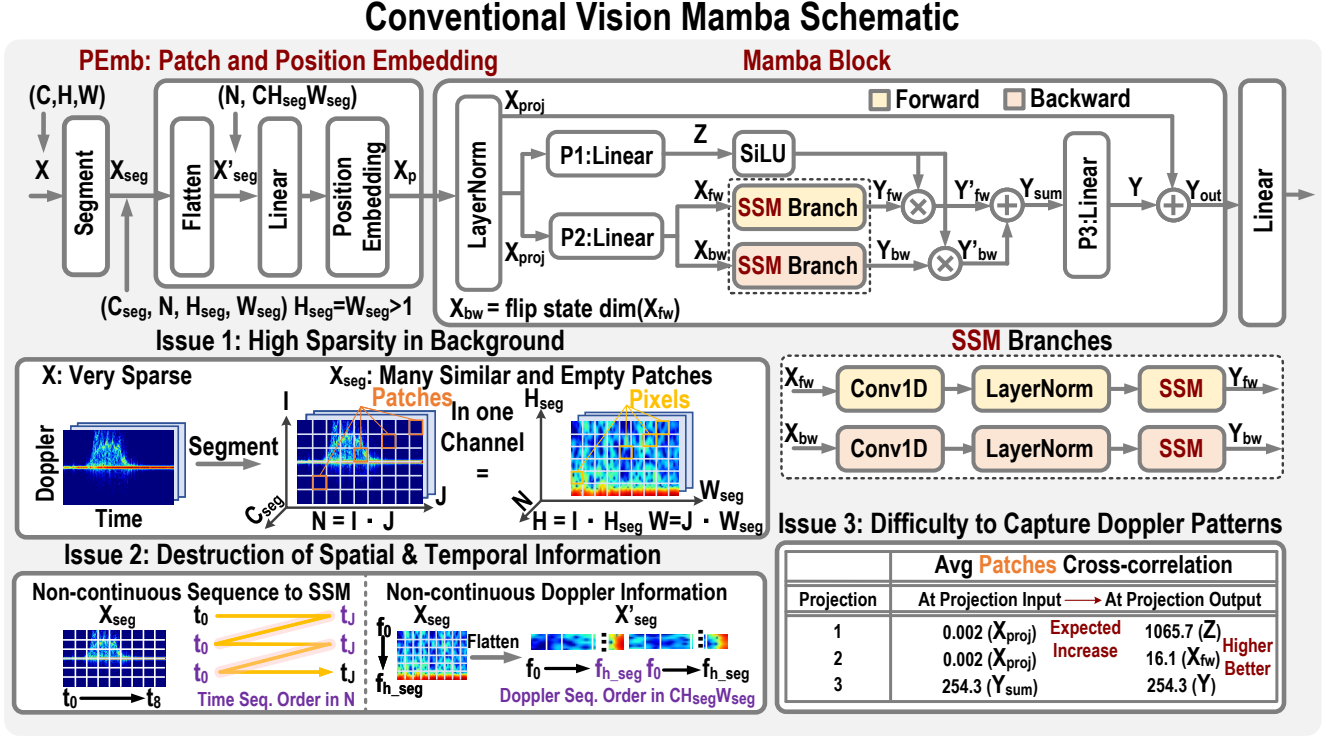


Fig. 1. The schematic of conventional Vision Mamba and its three potential issues while classifying the micro-Doppler-based human activity recognition.

FMCW radar data [30], though both demand significant #FLOP per inference. (169 M and 2.41 G, respectively). In continuous HAR, however, ViT appears to under-perform conventional CNN-based models, such as the first to the third blocks of AlexNet and ResNet [17]. SSM-based approaches [19] hit 99.82% accuracy on a non-continuous Continuous Wave (CW) dataset [30] with 8.7 M parameters and 1.22G #FLOP per inference.

III. ANALYSIS OF RADAR DATA FED TO ViM AND DESIGN MOTIVATION

To effectively combine the modeling strength of SSM and decrease computational complexity, it is crucial to consider the unique properties of micro-Doppler signatures. To illustrate this, we trace the data flow from input to SSM in Vision Mamba (ViM), highlighting issues specific to radar micro-Doppler-based HAR tasks. Other details will be explained in section IV. As shown in Fig. 1, classical ViM comprises three core components: patch and position embedding, Mamba block with bidirectional branches, and SSMs.

A. Issue 1: Micro-Doppler signatures exhibit significant sparsity.

The micro-Doppler signature $\mathbf{X} \in \mathbb{R}^{C \times H \times W}$ serves as input to the classifier, with the Doppler frequency dimension represented as the image height H and time as the image width W . The number of channels C may correspond to channels from multiple radar sensors or one of the RGB channels. Analysis of Dataset [31] CI4R reveals that \mathbf{X} exhibits an average

spectrogram sparsity of approximately 87%, as illustrated in Fig.1 Issue 1. In the subsequent *Segment* step, \mathbf{X} is divided into a matrix of smaller patches $\mathbf{X}_{seg} \in \mathbb{R}^{C \times I \times J \times H_{seg} \times W_{seg}}$, where H_{seg} and W_{seg} denote the height and width of each patch, respectively. Consequently, the number of patches per column is $I = \frac{H}{H_{seg}}$, and per row is $J = \frac{W}{W_{seg}}$. As depicted in Fig.1 Issue 1, many patches in \mathbf{X}_{seg} contain only background information and resemble one another, providing little discriminative detail regarding Doppler frequency and time within each patch.

B. Issue 2: Destruction of Spatial and Temporal Information.

Changes in Doppler frequency over time are critical for distinguishing various human activities. However, rectangular patch segmentation disrupts the relative positioning of Doppler frequency and time through two processes:

1) *Segment Undermines Temporal Interpretability in SSM, as Shown in Fig. 1, Issue 2 Left:* As illustrated in Fig.1 left, a patch with column index j can be interpreted as time point t_j , where $j = 0, 1, \dots, J$. During segmentation, the patch matrix of dimensions $I \times J$ is reshaped into a one-dimensional sequence $N = I \cdot J$. This reshaping results in a time point sequence of dimension N as $[t_0, t_1, \dots, t_J, t_0, t_1, \dots, t_J, \dots]$, represented by the yellow folded line in Fig.1 left. However, in a real-time sequence, t_J and t_0 are not continuous. When the dimension N remains unchanged from *Segment* to *SSMbranch*, and the SSM branches treat N as the direction of temporal evolution, the SSM encounters a discontinuous sequence. This discontinuity hinders its ability to discern significant features in the micro-Doppler signature.

2) *Flatten Compromises Spatial Information Integrity Across Time and Doppler Dimensions in Patches, as Shown in Fig. 1, Issue 2 Right:* Following segmentation, each patch is flattened into a vector:

$$\mathbf{X}'_{seg} = \text{Flatten}(\mathbf{X}_{seg}) \quad (1)$$

where $\mathbf{X}'_{seg} \in \mathbb{R}^{N \times CH_{seg}W_{seg}}$. A pixel with row index h_{seg} can be interpreted as Doppler frequency point $f_{h_{seg}}$, where $h_{seg} = 0, 1, \dots, H_{seg}$. The *Flatten* operation results in a Doppler point sequence in $H_{seg}W_{seg}$ as $[f_0, f_1, \dots, f_{h_{seg}}, f_0, f_1, \dots, f_{h_{seg}}, \dots]$, as shown in Fig. 1 left. However, $f_{h_{seg}}$ and f_0 are not continuous in the Doppler frequency sequence, disrupting the Doppler frequency features. This disruption also affects the time dimension within each patch.

In summary, the second issue encountered by conventional ViM is that Doppler and temporal information within H_{seg} and W_{seg} is compromised by flattening.

C. Issue 3: Challenges for Projection Layers in Capturing Doppler Patterns

Within the Mamba block, as shown in Fig. 1 top, the input \mathbf{X}_p first undergoes layer normalization to yield \mathbf{X}_{proj} , which is then split into two branches via linear projections *P1* and *P2*:

$$\mathbf{Z} = \mathbf{W}_{P1}\mathbf{X}_{proj} + \mathbf{b}_{P1}, \quad (2)$$

$$\mathbf{X}_{fw} = \mathbf{W}_{P2}\mathbf{X}_{proj} + \mathbf{b}_{P2}, \quad (3)$$

where the \mathbf{W} and \mathbf{b} terms are the weight matrices and bias vectors, respectively.

The projection operations are expected to extract Doppler frequency patterns over time and enhance the average cross-correlation between patches. This enhancement occurs because a high-performing classifier should recognize all Doppler-aligned vectors of a specific activity as a cohesive and highly relevant unit. However, the averaged cross-correlation between patches shows limited improvement from conventional projections *P1* and *P2*. For instance, in Dataset CI4R [31], the average patch cross-correlation is 0.008 before projections 1 and 2. After projections 1 and 2, they rise to 77.9 and 0.4, respectively. In contrast to the improvements achieved through our proposed Conv1D projection (detailed later in Section IV-C), the linear layers in the conventional ViM architecture demonstrate limited capability to enhance cross-correlation between patches and consistently identify all time bins as components of the same action.

The tensors \mathbf{X}_{fw} and \mathbf{X}_{bw} resulting from the projections *P1* and *P2* are then passed through SSM branches. The outputs from both directions are combined using a gating mechanism modulated by the SiLU-activation to produce the gated output \mathbf{Y}_{sum} . This gated output passes through projection layer *P3*, which is linear in the conventional ViM, and is added to the input via a residual connection:

$$\mathbf{Y}_{out} = \mathbf{W}_{P3}\mathbf{Y}_{sum} + \mathbf{b}_{P3} + \mathbf{X}_{proj}, \quad (4)$$

Before and after projection 3, again using Dataset CI4R as an example, the average patch cross-correlation is 160.1 and

75.5, respectively. Essentially, the averaged cross-correlation between patches is even decreased by the conventional projection layer 3, posing a challenge to achieve good classification performance.

In the analysis of Issue 3, to compute the averaged patch cross-correlation, we first trained a model to its optimal performance, then duplicated and froze its parameters. By re-feeding the data into the frozen model, we calculated the averaged patch cross-correlation during inference. This averaged patch cross-correlation also accounts for different batches (classes). For example, with $\mathbf{X}_{proj} \in \mathbb{R}^{B \times N \times D}$, each patch is labeled with its index n in \mathbf{X}_{seg} . The averaged patch cross-correlation is defined as:

$$Corr_{avg} = \frac{1}{B} \left(\frac{1}{N} \sum_{n=1}^N \left(\frac{1}{N} \sum_{n'=1}^N \left(corr(\mathbf{X}_{proj}(\mathbf{b}, \mathbf{n}), \mathbf{X}_{proj}(\mathbf{b}, \mathbf{n}')) \right) \right) \right) \quad (5)$$

where the correlation between two vectors of equal length is computed as:

$$corr(\mathbf{A}, \mathbf{B}) = \sum_{m=0}^M \sum_{m'=0}^M \mathbf{A}[m] \cdot \mathbf{B}[m + m'] \quad (6)$$

IV. PROPOSED RADMAMBA

To overcome the aforementioned challenges and issues, we propose a micro-Doppler-oriented RadMamba architecture, illustrated in Fig. 2. These modifications to the conventional approach include channel fusion and down-sampling, Doppler-aligned segmentation, and modified Mamba block rMamba.

A. Solution 1: Channel Fusion and Downsample

To tackle the issue of many similar and empty patches caused by high sparsity inherent in micro-Doppler signatures input $\mathbf{X} \in \mathbb{R}^{C \times H \times W}$, we introduce a preprocessing pipeline prior to the segmentation stage, as depicted in Fig. 2 *Chan-DS*: Channel Fusion and Downsample.

$$\mathbf{X}_{c-d} = \text{Chan-DS}(\mathbf{X}) \quad (7)$$

where $\mathbf{X} \in \mathbb{R}^{C_{c-d} \times H_{c-d} \times W_{c-d}}$, $H_{c-d} < H$, $W_{c-d} < W$ is the input micro-Doppler signature after the channel fusion and downsample for each batch. The architecture of the *Chan-DS* block is as follows:

$$\begin{aligned} \text{Chan-DS} = & [(\text{Conv2D}, \text{BatchNorm}) \times L, \\ & \text{Maxpool2D}, \\ & \text{Maxpool1D}, \\ & \text{Avgpool1D (optional)}] \end{aligned}$$

where $L = 1, 2$. The Two-Dimensional (2D) convolutional layer and batch normalization layer mix channel information and extract preliminary features from the input tensor \mathbf{X} . A 2D max pooling layer and a One-Dimensional (1D) max pooling layer reduces spatial dimensions. Optionally, an additional 1D average pooling layer with a kernel height as one and kernel width larger than 1, for example (1, 4), further downsamples the time dimension if the data sparsity along the time axis,

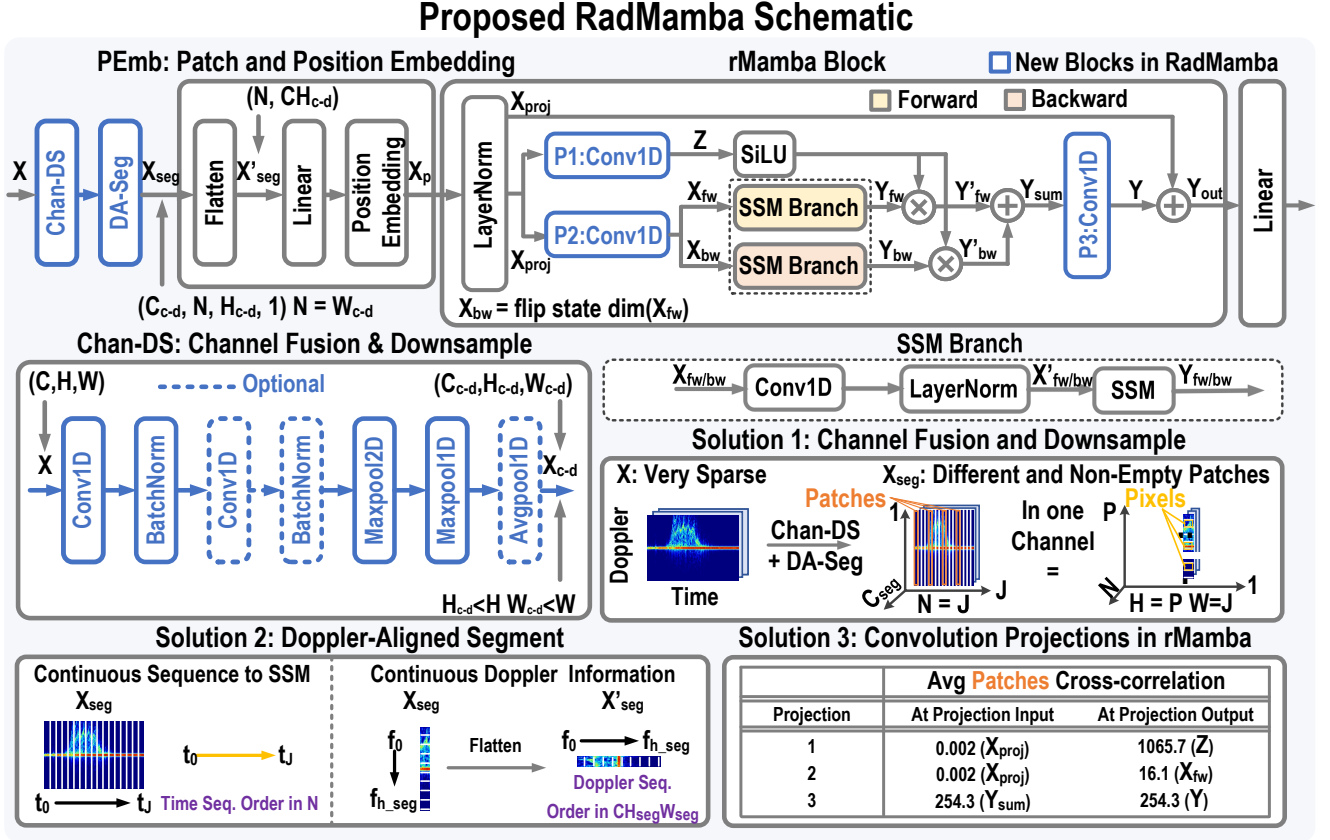


Fig. 2. The schematic of the proposed RadMamba architecture and its novel solutions for radar micro-Doppler-based classification.

influenced by the Pulse Repetition Interval (PRI) of the radar and pre-processing to generate the input, is excessive.

In combination with the Doppler-Aligned Segment explained in the next subsection IV-B, this method avoids the issue of having many similar and empty patches of data. Moreover, the down-sampling decreases the available size for patch segmentation, which enhances the energy-efficient design.

B. Solution 2: Doppler-Aligned Segment and Patch Embedding

To maintain the temporal and Doppler location information embedded in micro-Doppler signatures, we propose a new patch segmentation strategy, as shown in Fig. 2 Solution 2 Doppler-Aligned Segment, *DA-Seg*:

$$\mathbf{X}_{seg} = DA-Seg(\mathbf{X}_{c-d}) \quad (8)$$

Specifically, we define patches with a height of $H_{seg} = H_{c-d}$ (the full Doppler dimension) and a width of $W_{seg} = 1$ (a single time bin of the spectrogram).

This approach ensures that the temporal evolution of state sequence N remains as $[t_0, t_1, \dots, t_J]$ and continuous as time sequence W . When the data is sent to the SSM, as depicted in Fig. 2 Solution 2 left, this method avoids the loss of critical temporal information that conventional square patches of the ViM might face.

Moreover, this segmentation approach results in a pixel sequence dimension $CH_{seg}W_{seg} = H_{c-d}$ of \mathbf{X}'_{seg} that preserves the frequency pattern as $[f_0, f_1, \dots, f_{h_{seg}}]$, during Flatten operations within each Doppler bin, as shown in Fig. 2 Solution 2 left, as:

$$\mathbf{X}'_{seg} = Flatten(\mathbf{X}_{seg}) = \mathbf{X}_{seg} \quad (9)$$

C. Solution 3: Convolution Projections in rMamba Blocks

Finally, to increase the capability of projection layers to capture the Doppler patterns, we replace the conventional linear projection layers within the conventional Mamba block with 1D convolutional layers, as highlighted in Fig. 2 rMamba Block, in the blue boxes on the top-right part of the figure.

Within the rMamba block, the linear projections $P1$ and $P2$ are replaced by *Conv1D* layer as:

$$\mathbf{Z} = Conv1D_{P1}(\mathbf{X}_{proj}), \quad (10)$$

$$\mathbf{X}_{fw} = Conv1D_{P2}(\mathbf{X}_{proj}), \quad (11)$$

$$\mathbf{X}_{bw} = \text{flip state dim}(\mathbf{X}_{fw}), \quad (12)$$

where $\mathbf{Z}, \mathbf{X}_{fw}, \mathbf{X}_{bw} \in \mathbb{R}^{N \times dim}$. Both *Conv1D* operations utilize a kernel size (in channels, out channels, kernel size) = $(dim, dim, 3)$.

When \mathbf{X}_{fw} and \mathbf{X}_{bw} pass through the SSM branches with architecture of:

$$[Conv1D_{fw/bw}, LayerNorm_{fw/bw}, SSM_{fw/bw}] \quad (13)$$

The $\text{Conv1D}_{fw/bw}$ has weights of shape $(dim, dim, 1)$, reflecting a kernel size of 1, and operates on the sequence of dimensions (N, dim) .

The outputs from both directions are combined using a gating mechanism modulated by the SiLU-activated Z and summed:

$$\mathbf{Y}'_{fw/bw} = \mathbf{Y}_{fw/bw} \odot \text{SiLU}(\mathbf{Z}) \quad (14)$$

$$\mathbf{Y}_{sum} = \mathbf{Y}'_{fw} + \mathbf{Y}'_{bw} \quad (15)$$

where \odot denotes element-wise multiplication. Additionally, in our proposed *rMamba*, the projection layer $P3$ is also replaced by *Conv1D*, so that:

$$\mathbf{Y}_{out} = \text{Conv1D}_{P3}(\mathbf{Y}_{sum}) + \mathbf{X}_{proj}, \quad (16)$$

where the final *Conv1D* has weights of dimensions $(dim, dim, 1)$ and transforms the combined sequence back to (N, dim) .

These convolutional layers enable the model to capture subtle variations in Doppler-span changes over time, which are crucial to describe the kinematic evolution of the different activities to be classified. Also, let us take Dataset CI4R as a comparison reference and follow the method to calculate cross-correlation as explained in Section III Issue 3. While passing through RadMamba, the average time bin cross-correlation is 0.002 before projection 1 and 2.

Then, compared to conventional linear projection, the convolution projection 1 increased the averaged cross correlation gap between projection input and output from 77.9 to 1065.7. The convolutional projection 2 increased this gap from 0.4 to 16.1. The convolutional projection 3 increased the average time cross-correlation from 245.3 to 356.4, while the linear projection 3 decreased this number. This enhancement significantly improves the model's sensitivity to Doppler patterns between patches and makes it easier to regard all patches as one activity, thereby boosting classification performance.

D. Selective State-Space Modeling for Micro-Doppler Sequences

The SSM is a significant layer in *rMamba* enables efficient sequence modeling for the dynamic nature of micro-Doppler signatures. As shown in Fig. 3 (a), the discrete SSM is defined as:

$$\mathbf{h}[n] = \bar{\mathbf{A}}[n]\mathbf{h}[n-1] + \bar{\mathbf{B}}[n]\mathbf{x}[n], \quad (17)$$

$$\mathbf{y}[n] = \mathbf{C}\mathbf{h}[n] + \mathbf{D}\mathbf{x}[n], \quad (18)$$

where the state transition $\bar{\mathbf{A}}$ and the input matrices dimension $\bar{\mathbf{B}}$ are discretized from corresponding matrices \mathbf{A} and \mathbf{B} in continuous SSM by a learnable step size Δ as shown in Fig. 3 (b):

$$\bar{\mathbf{A}} = \exp(\Delta \cdot \mathbf{A}), \quad (19)$$

$$\bar{\mathbf{B}} = \left(\int_0^\Delta \exp(\mathbf{A}\tau) d\tau \right) \mathbf{B}, \quad (20)$$

The input of the SSM branches in the proposed *rMamba* block are tensors $\mathbf{X}_{fw/bw} \in \mathbb{R}^{N \times dim}$; after *Conv1D* and *LayrNorm* in SSM branch, this is termed as $\mathbf{X}'_{fw/bw} \in \mathbb{R}^{N \times dim}$.

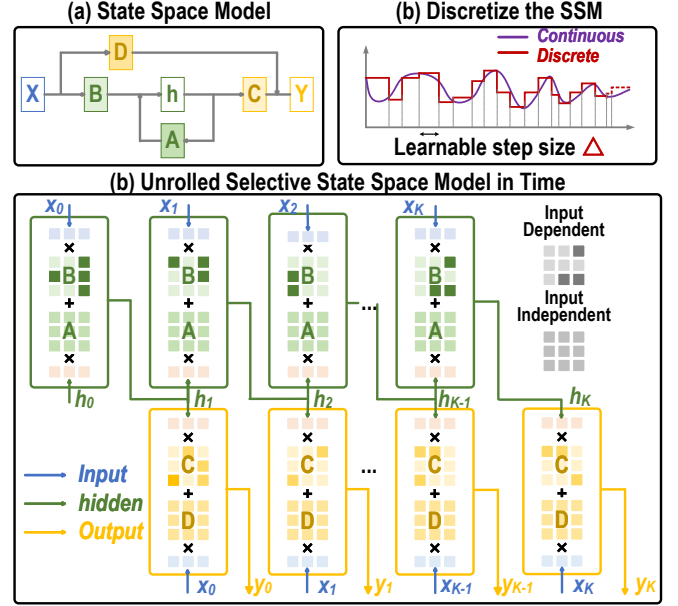


Fig. 3. The architecture of State Space Model in RadMamba.

Therefore, the dimension of the discretized state transition $\bar{\mathbf{A}}$ is $N \times dim \times dim_s$ and the input matrices dimension $\bar{\mathbf{B}}$ is $N \times N \times dim_s$, respectively. While N equals the time dimension in micro-Doppler signatures, the input matrices $\bar{\mathbf{B}}$ captures how the Doppler-aligned vector influences the state $\mathbf{h}[n]$, and the discretized state transition weight $\bar{\mathbf{A}}$ capture how the last state $\mathbf{h}[n-1]$. Moreover, the matrices $\mathbf{C} \in \mathbb{R}^{N \times dim_s}$ translate the current state $\mathbf{h}[n]$ to the output. The skip matrices $\mathbf{D} \in \mathbb{R}^{dim}$ add weighted input directly to output of SSM, which helps the recurrent part focus on the temporal evolution.

The selective mechanism in the SSM introduces input-dependent parameterization that enhances adaptability as shown in Fig. 3 (c). The parameters \mathbf{B} , \mathbf{C} , and Δ are dynamically generated from the input sequence via linear projections:

$$\mathbf{B} = \mathbf{W}_B \mathbf{X}, \quad (21)$$

$$\mathbf{C} = \mathbf{W}_C \mathbf{X}, \quad (22)$$

$$\Delta = \text{Softplus}(\mathbf{W}_\Delta \mathbf{X}), \quad (23)$$

where \mathbf{W}_B and \mathbf{W}_C are weights of dimension (dim, dim_s) . The Δ computation involves a linear layer with weights (dim, dt_rank) followed by a projection to (N, dim) via weights (dt_rank, dim) , where dt_rank is a hyperparameter controlling the rank of the dynamic tensor. The Softplus activation ensures positive step sizes, implemented as $\text{Softplus}(x) = \log(1 + \exp(x))$.

E. Overall Architecture

To summarize the method, the proposed RadMamba pipeline in pseudo-code is presented in Algorithm I. The patch embedding in *PEmb* follows the method in [15] and the position embedding method is a sinusoidal position encoding. [32].

Algorithm 1 Proposed RadMamba Pipeline**Input:** Micro-Doppler Signature $\mathbf{X} \in \mathbb{R}^{C \times H \times W}$ **Parameters:** dim, dim_s, dt_rank **Output:** Classification Result $\mathbf{F} \in \mathbb{R}^Q$, where Q is the number of classes

- 1: **Channel Fusion and Downsample:**
- 2: $\mathbf{X}_{c-d} = Chan-DS(\mathbf{X}), \mathbf{X}_{c-d} \in \mathbb{R}^{C_{c-d} \times H_{c-d} \times W_{c-d}}$
- 3: **Doppler-Aligned Segmentation:**
- 4: $\mathbf{X}_{seg} = DA-Seg(\mathbf{X}_{c-d}), \mathbf{X}_{seg} \in \mathbb{R}^{C_{c-d} \times N \times H_{c-d}}$
- 5: **Patch and Position Embedding:**
- 6: $\mathbf{X}'_p = PEmb(\mathbf{X}_{seg}), \mathbf{X}'_p \in \mathbb{R}^{N \times D}$
- 7: **rMamba Block:**
- 8: $\mathbf{Y}_{out} = rMamba(\mathbf{X}_p), \mathbf{Y}_{out} \in \mathbb{R}^{N \times dim}$
- 9: **Classify:**
- 10: $\mathbf{F} = \mathbf{W}_{out} \mathbf{Y}_{out}, \mathbf{F} \in \mathbb{R}^Q$

TABLE I
INFORMATION OF DIFFERENT RADAR-BASED ACTIVITY RECOGNITION
DATASETS USED IN THIS WORK.

Datasets	DIAT	CI4R	UoG2020
Continuous	No	No	Yes
Classes	6	11	6
Sensor	X-band CW	IWR1443 FMCW	FMCW
Freq.(GHz)	10	77	5.8
Resolution	224×224	224×224	240×1471
BW(MHz)	-	750	400
Length per sample (s)	3	20	35
Train Samples	2646	528	39
Test Samples	759	132	6
Sliding Window			224

V. OPEN-SOURCE DATASETS AND PREPROCESSING FOR RADAR-BASED HAR

To evaluate the efficacy of our proposed RadMamba framework, we utilize three distinct radar datasets. This section describes these datasets, namely the CW non-continuous Dataset DIAT, FMCW non-continuous Dataset CI4R, and FMCW continuous Dataset UoG2020, along with their respective preprocessing steps. More details on these datasets are summarized in Tab. I. Here the word ‘continuous’ refers to samples of data where sequences of human activities are performed one after the other in a continuous manner.

A. Dataset DIAT: X-Band CW Radar with Discrete Activity Instances [30]

This dataset was collected using an X-band CW radar operating at a frequency of 10 GHz. It encompasses data from 30 human subjects performing ‘suspicious’ activities at ranges spanning 10 meters to ± 0.5 kilometers over 3-second durations, resulting in an imbalanced set of 3,780 spectrogram samples of shape (3, 244, 244) across six activity classes. Preprocessing adheres to the methodology outlined in [30]. To facilitate a fair comparison with previous works, the dataset is partitioned into 70% training, 10% validation, and 20% test sets within each class, maintaining class-specific balance for reliable performance evaluation.

B. Dataset CI4R: Short-Range FMCW Radar for Multi-Class Activity Recognition [31]

The experiments of the second dataset employ a Texas Instruments IWR1443 FMCW radar, operating at 77 GHz with a bandwidth of 750 MHz. It includes data from six participants, varying in age, height, and weight, performing 11 distinct activities and ambulatory gaits. Each participant executed 10 repetitions per activity, yielding 60 samples per class per sensor, as detailed in [31]. Preprocessing involves applying a 256-point short-time Fourier transform (STFT) with a context window length to convert the raw radar signals into a 2D micro-Doppler representation of shape (1, 244, 244). The dataset is split with an 8:2 training-to-test ratio, ensuring sufficient data for model optimization and evaluation.

C. Dataset UoG2020: Continuous FMCW Radar for Realistic HAR Sequences [27]

Representing a leap in complexity, this dataset was acquired using an FMCW radar operating at 5.8 GHz with a 400 MHz bandwidth. It comprises data from 15 participants (14 males, 1 female, aged 21–35) performing six basic activities within continuous 35-second sequences. These activities are organized into three distinct sequential orders, with participants granted autonomy in selecting transition points between consecutive activities and determining trajectories for translational tasks, as described in [27]. The resulting micro-Doppler signatures are preprocessed into (1, 240, 244) 2D frames, with two participants’ data designated as the test set, while the remaining 13 contribute to training, providing a challenging benchmark for continuous sequence modeling.

VI. EXPERIMENTAL SETUP

A. Training Hyperparameter

Training is conducted using the ADAMW optimizer [33], [34], paired with the ReduceLROnPlateau scheduler to adjust the learning rate based on test performance adaptively. For Dataset DIAT, the initial learning rate is set to 1×10^{-4} , with a batch size of 16, and training proceeds for 50 epochs. For Dataset CI4R, RadMamba employs an initial learning rate of 5×10^{-3} , while the baseline models use 1×10^{-4} , with a batch size of 16 over 100 epochs, reflecting the dataset’s increased complexity and sample size. For Dataset UoG2020, the initial learning rate is 5×10^{-5} , with a larger batch size of 256 and 50 epochs, processing continuous sequences with a frame length of 224 and a stride of 1 to capture temporal dependencies effectively. All experiments are executed on a single NVIDIA RTX 4090 GPU.

To account for training variability, all models, including RadMamba, are trained and evaluated ten times with distinct seeds, reporting in the following analysis the mean and standard deviation of performance metrics in the model size swept experiment.

B. Network Structure

The classification performance of RadMamba is evaluated against a suite of established models, selected for their

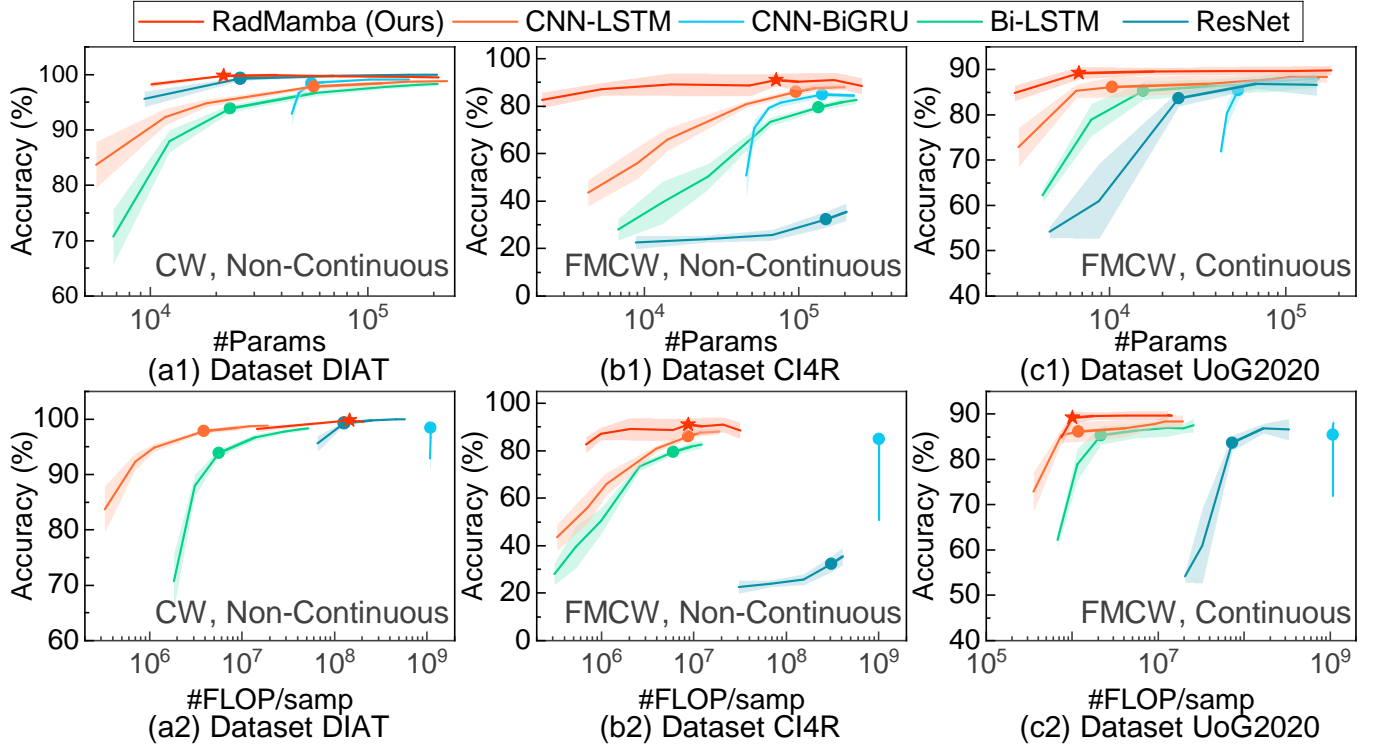


Fig. 4. Accuracy vs. number of parameters (1) and number of #FLOP per inference (2) on: (a) Dataset DIAT (b) Dataset CI4R (c) Dataset UoG2020

TABLE II
NETWORK ARCHITECTURE OF MODELS USED IN THIS WORK

Model	Swept Hidden Size (dim for RadMamba)
ResNet	[5, 7, 12, 20, 30]
Bi-LSTM	[1, 2, 4, 10, 20, 28, 34]
CNN-LSTM	[2, 4, 6, 16, 28, 34, 46]
CNN-Bi-GRU	[1, 2, 4, 6, 16, 28]
RadMamba Dataset DIAT	[8, 16, 32, 64, 80]
RadMamba Dataset CI4R	[8, 16, 32, 64, 80, 96, 128, 160]
RadMamba Dataset UoG2020	[8, 16, 20, 24, 32]

TABLE III
SPECIFIED NETWORK ARCHITECTURE VARIATIONS OF RADMAMBA

Datasets	dim_s	dt_rank	Chan. Fusion	DS Redu. Factor
Dataset DIAT	1	2	[2, (16, 3, 3)]	(2, 2)
Dataset CI4R	4	0	[1, (1, 3, 3)]	(2, 8)
Dataset UoG2020	16	4	[1, (1, 3, 3)]	(2, 32)

proven efficacy across CNN, RNN, and hybrid architectures: ResNet [35], Bi-LSTM [27], CNN-LSTM [13], and CNN-Bi-GRU [14]. To explore the impact of model scaling, we conducted a model size swept experiment, varying the hidden dimensions as shown in Tab. II. These sizes are chosen to capture the full spectrum of performance trends as model capacity increases, providing insights into scalability and efficiency.

Notably, the CNN-Bi-GRU model, originally designed for distributed radar systems in [14], exhibits a larger parameter count, though its channel fusion approach may not generalize across all datasets.

For RadMamba, specific configurations of the channel fusion and down-sampling blocks, as well as the SSM parameters, are tailored to each dataset to optimize micro-Doppler

processing as shown in Tab. III, where the ‘channel fusion’ column specifies $[L, (C_{c-d}, H_k, W_k)]$, where L is the number of channel fusion blocks and the C_{c-d}, H_k, W_k are channel, kernel height, kernel width of Conv2D layer, respectively. The ‘DS Redu. Factor’ denotes the reduction factors $(H/H_{c-d}, W/W_{c-d})$.

For transformer-based and SSM-based models such as FML-ViT [16], LW-ViT [21], and ActivityMamba [19], we adopt their reported results as optimal outcomes under minimal model sizes, as dimension definitions may vary and are not always fully specified in the original works.

VII. RESULTS AND DISCUSSION

A. Model Scaling and Efficiency Analysis

The model size swept results, illustrated in Figure 4, compare accuracy against the number of parameters from 2k to 150k and #FLOP per inference across Datasets DIAT, CI4R, and UoG2020 between previous models ResNet, Bi-LSTM, CNN-Bi-GRU, and CNN-LSTM and the proposed RadMamba.

For Dataset DIAT, as presented in Fig. 4 (a1) and (a2), RadMamba achieves a peak accuracy of 99.8% with only 21.7k parameters. However, RadMamba overfits with a model size larger than 21.7k because the dataset is very simple and the accuracy is close to 100%. In contrast, ResNet’s accuracy increases steadily with model size, reaching 99.9% with 208.1k parameters, yet it requires nearly ten times the parameters of RadMamba for slightly lower performance. On Dataset CI4R, as shown in Fig. 4 (b1) and (b2), RadMamba consistently outperforms previous models across a

TABLE IV
MEAN AND STANDARD DEVIATION OF CLASSIFICATION ACCURACY PERFORMANCE ACROSS SEED 0 TO 9 OF DIFFERENT NN-BASED RADHAR MODELS EVALUATED WITH THREE DIFFERENT RADAR SETTINGS ALONGSIDE THEIR MODEL SIZE AND FLOATING-POINT OPERATIONS PER INFERENCE SAMPLE (FLOP/INF.)

Classifiers		Dataset DIAT [30] (CW, Non-continuous)			Dataset CI4R [31] (FMCW, Non-continuous)			Dataset UoG2020 [27] (FMCW, Continuous)		
		#params (k)	#FLOP/Inf. ^a (M)	Accuracy (%)	#params (k)	#FLOP/Inf. ^a (M)	Accuracy (%)	#params (k)	#FLOP/Inf. ^a (M)	Accuracy (%)
ResNet ^b	[35]	69.4	253.3	99.8±0.16	150.7	310.2	32.3±3.35	24.7	72.8	83.6±1.73
Bi-LSTM	[27]	23.3	5.6	93.9±0.68	134.4	6.0	79.4±1.23	15.5	2.1	85.3±2.01
CNN-LSTM	[13]	115.3	8.7	98.4±0.33	96.5	8.7	86.1±1.32	10.3	1.2	86.1±2.22
CNN-Bi-GRU	[14]	55.0	1090.1	98.5±0.41	142.8	1013.0	84.9±1.11	53.6	1082.0	85.4±2.19
FML-ViT ^c	[16]	-	-	-	~2700	169.0	~92.0	-	-	-
LW-ViT ^c	[21]	-	-	-	769	~2410	~92.0	-	-	-
ActivityMamba ^c	[19]	~8700.0	~1220.0	99.8	-	-	-	-	-	-
RadMamba (Ours)		21.7	145.6	99.8±0.12	71.4	8.8	91.2±2.57	6.7	1.0	89.3±1.38
RadMamba (Ours)		10.1	14.5	98.2±0.46	47.9	6.0	88.8±4.58	17.7	1.8	89.6±0.78

^a #FLOP/Inf. is the number of Floating point operations per inference.

^b This ResNet only retains the structure of ResNet18 from the first layer to the end of the second residual block. The relative multiples of channels between convolution layers remain unchanged, but the size of the minimum channel can be adjusted.

^c The '~' indicates that these results are approximated from the references [16], [19], [21].

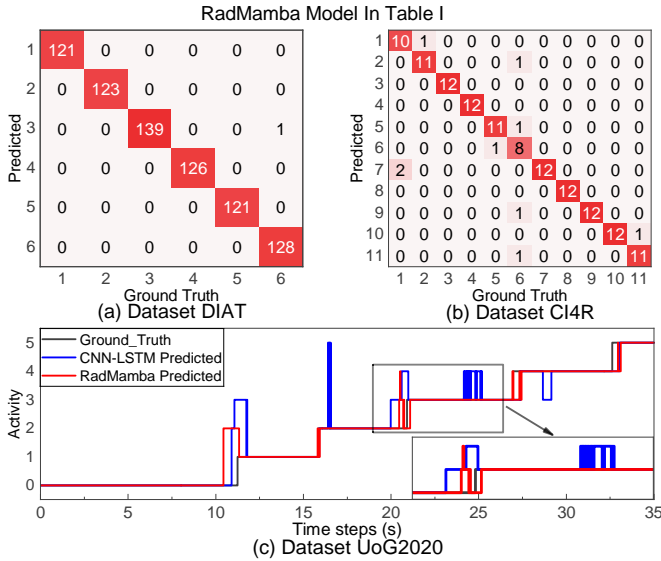


Fig. 5. Comparison between ground truth and best prediction of RadMamba model with the configuration in Table I on (a) Dataset DIAT; (b) Dataset CI4R; (c) Dataset UoG2020.

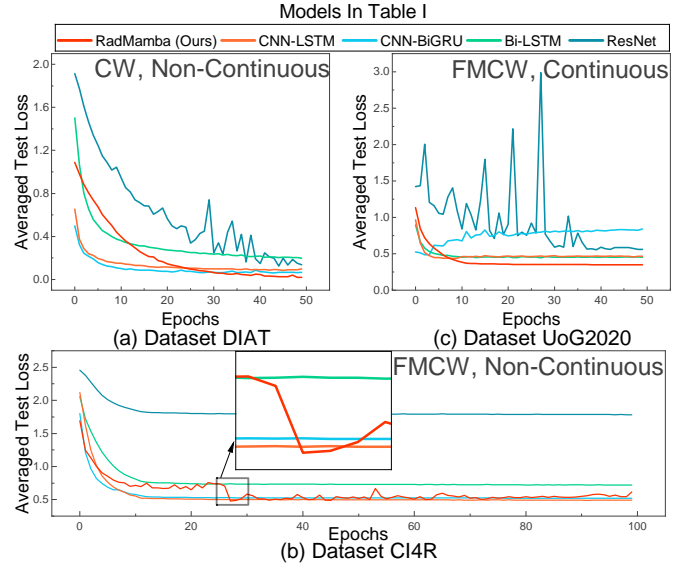


Fig. 6. Averaged test loss across 10 random seeds vs. Epochs during training of models with configuration in Table I on (a) Dataset DIAT; (b) Dataset CI4R; (c) Dataset UoG2020.

range of parameter configurations in efficiency, maintaining superior accuracy with fewer parameters and #FLOP/Inf. Similarly, for Dataset UoG2020 shown in Fig. 4 (c1) and (c2), RadMamba still records a higher accuracy for continuous activities scenarios with fewer #FLOP/Inf., outperforming larger and more computationally intensive models in efficiency and effectiveness.

These trends, as depicted in the figure, affirm RadMamba's capability to achieve superior accuracy across diverse radar modalities while drastically reducing both parameter count and #FLOP/Inf., positioning it as an optimal solution for lightweight, real-time human activity recognition.

B. Comparison with Previous Works

The experimental results detailed in Table IV highlight the superior performance of our proposed RadMamba model across multiple radar-based human activity recognition datasets.

On Dataset DIAT, which utilizes CW radar in a non-continuous setting, RadMamba achieved an accuracy of 99.8% with a standard deviation of $\pm 0.12\%$, using only 21.7k parameters and requiring 145.6 million #FLOP/Inf. per sample. This demonstrates its capability to match the state-of-the-art accuracy of previous models while being significantly more parameter-efficient compared to ~8700k parameters and computationally lighter compared to ~1220M #FLOP per inference. The CNN-LSTM with 8.7M #FLOP per inference achieves better accuracy of 98.4% than 98.2% from

TABLE V
ABLATION STUDY WITH PROGRESSIVE TECHNIQUES (DENOTED BY **TECH.**) OF NEW BLOCKS IN RADMAMBA ACROSS SEED 0 TO 5, EVALUATED WITH THREE DIFFERENT RADAR SETTINGS ALONGSIDE THEIR NUMBER OF PARAMETERS

Row	Tech. 1: Proj. Layer	Tech. 2: Patch Size	Dataset DIAT			Dataset CI4R			Dataset UoG2020		
			Tech. 3: Down-sample.	Accuracy (%)	#Params (k)	Tech. 3: Down-sample.	Accuracy (%)	#Params (k)	Tech. 3: Down-sample.	Accuracy (%)	#Param (k)
1 (Conventional)	1 linear layer	$(H_{seg}, W_{seg})^a$	(1, 1)	93.5 \pm 1.06	11.3	(1, 1)	61.9 \pm 2.55	40.6	(1, 1)	71.2 \pm 2.10	4.2
2			-	-	-	\Downarrow (8, 2)	71.6 \pm 2.42	40.6	\Downarrow (8, 2)	80.1 \pm 2.07	4.2
3			(2, 2)	99.6 \pm 0.06	11.3	\Leftrightarrow (2, 8)	63.0 \pm 7.75	40.6	\Leftrightarrow (2, 32)	66.9 \pm 2.01	4.2
4		$(1, W_{c-d})$	(1, 1)	87.7 \pm 1.25	39.3	(1, 1)	67.9 \pm 0.76	54.9	(1, 1)	72.6 \pm 2.20	7.6
5			-	-	-	\Downarrow (8, 2)	65.2 \pm 2.73	45.8	\Downarrow (8, 2)	67.7 \pm 1.27	5.5
6			(2, 2)	98.5 \pm 0.43	21.4	\Leftrightarrow (2, 8)	77.3 \pm 2.80	38.9	\Leftrightarrow (2, 32)	64.0 \pm 1.26	3.6
7		$(H_{c-d}, 1)$	(1, 1)	96.9 \pm 0.52	39.3	(1, 1)	88.4 \pm 0.76	54.9	(1, 1)	83.9 \pm 1.85	7.8
8			-	-	-	\Downarrow (8, 2)	84.6 \pm 4.12	38.9	\Downarrow (8, 2)	84.3 \pm 1.88	4.1
9			(2, 2)	99.9 \pm 0.00	21.4	\Leftrightarrow (2, 8)	86.5 \pm 4.35	45.8	\Leftrightarrow (2, 32)	84.2 \pm 2.00	5.7
10	3 linear layer ^b	$(H_{seg}, W_{seg})^a$	(1, 1)	92.6 \pm 0.98	11.6	(1, 1)	40.1 \pm 11.98	66.2	(1, 1)	70.6 \pm 2.12	5.2
11			-	-	-	\Downarrow (8, 2)	69.9 \pm 2.99	66.2	\Downarrow (8, 2)	78.2 \pm 3.66	5.2
12			(2, 2)	99.5 \pm 0.10	11.6	\Leftrightarrow (2, 8)	57.8 \pm 9.64	66.2	\Leftrightarrow (2, 32)	68.5 \pm 1.50	5.2
13		$(1, W_{c-d})$	(1, 1)	88.8 \pm 2.42	39.6	(1, 1)	48.3 \pm 9.80	80.5	(1, 1)	70.8 \pm 2.43	8.6
14			-	-	-	\Downarrow (8, 2)	43.3 \pm 8.54	71.4	\Downarrow (8, 2)	65.2 \pm 1.48	6.6
15			(2, 2)	98.7 \pm 0.32	21.7	\Leftrightarrow (2, 8)	72.4 \pm 3.12	64.5	\Leftrightarrow (2, 32)	64.0 \pm 2.16	4.7
16		$(H_{c-d}, 1)$	(1, 1)	97.2 \pm 0.26	39.6	(1, 1)	85.3 \pm 1.27	80.5	(1, 1)	83.6 \pm 1.04	8.9
17			-	-	-	\Downarrow (8, 2)	83.9 \pm 1.71	64.5	\Downarrow (8, 2)	83.2 \pm 1.64	5.1
18			(2, 2)	99.8 \pm 0.06	21.7	\Leftrightarrow (2, 8)	85.3 \pm 2.67	71.4	\Leftrightarrow (2, 32)	85.2 \pm 1.16	6.7
19	1 conv1d layer ^c	$(H_{seg}, W_{seg})^a$	(1, 1)	93.8 \pm 1.14	11.6	(1, 1)	65.5 \pm 3.30	66.2	(1, 1)	75.3 \pm 2.34	5.2
20			-	-	-	\Downarrow (8, 2)	75.0 \pm 2.45	66.2	\Downarrow (8, 2)	81.0 \pm 2.10	5.2
21			(2, 2)	99.6 \pm 0.15	11.6	\Leftrightarrow (2, 8)	70.7 \pm 3.23	66.2	\Leftrightarrow (2, 32)	74.3 \pm 2.31	5.2
22		$(1, W_{c-d})$	(1, 1)	90.1 \pm 1.72	39.6	(1, 1)	70.7 \pm 3.43	80.5	(1, 1)	76.4 \pm 2.77	8.6
23			-	-	-	\Downarrow (8, 2)	69.3 \pm 3.09	71.4	\Downarrow (8, 2)	74.4 \pm 3.26	6.6
24			(2, 2)	98.9 \pm 0.13	21.7	\Leftrightarrow (2, 8)	79.0 \pm 2.42	64.5	\Leftrightarrow (2, 32)	68.8 \pm 2.08	4.7
25		$(H_{c-d}, 1)$	(1, 1)	96.8 \pm 0.86	39.6	(1, 1)	87.9 \pm 0.36	80.5	(1, 1)	84.5 \pm 0.77	8.9
26			-	-	-	\Downarrow (8, 2)	85.6 \pm 3.16	64.5	\Downarrow (8, 2)	84.4 \pm 2.05	5.1
27 (Ours)			(2, 2)	99.8 \pm 0.11	21.7	\Leftrightarrow (2, 8)	89.6 \pm 3.69	71.4	\Leftrightarrow (2, 32)	88.6 \pm 1.46	6.7

^a (H_1, W_1) equals to (7, 7) for Dataset DIAT and B, (5, 7) for Dataset UoG2020 due to the different image size of these datasets.

^b This option replaces projections 1 and 2 from a single linear layer to three linear layers.

^c The kernel size for projection 1 and 2 is $(dim, 3, 3)$, and for projection 3 is $(dim, 1, 1)$.

RadMamba with 14.5M #FLOP per inference. However, take 45nm technology for example, the energy consumption for 8kB SRAM memory access of one 32-bit floating point parameter and one 32-bit floating point computing operation is 5.0pJ and 4.6pJ [36]. With $11\times$ larger model and around half #FLOP per inference, it's hard for CNN-LSTM to be more energy-efficient than RadMamba.

For Dataset CI4R, employing FMCW radar in a non-continuous scenario with 11 activities, RadMamba attained an accuracy of 91.2% with a standard deviation of $\pm 2.57\%$, leveraging 71.4 thousand parameters. This performance outperforms previous models shown in Tab. IV. Moreover, it remains competitive with the state-of-the-art of previous models while requiring substantially fewer computational resources (8.8M #FLOP/Inf. vs. 169M to 2410M #FLOP/Inf.), showcasing its ability to excel in more complex activity recognition tasks with minimal computational overhead. Moreover, compared to the Bi-LSTM model with lowest arithmetic intensity in table, RadMamba outperforms Bi-LSTM accuracy of 9.4% with 86.5k less parameters and same #FLOP per inference of 6.0M.

On Dataset UoG2020, which involves FMCW radar in a continuous setting with 6 activities, RadMamba recorded an accuracy of 89.3% with a standard deviation of $\pm 1.38\%$, utilizing 6.7 thousand parameters and 1.3M #FLOP per inference. With an even smaller model size and more complicated task compared to Datasets DIAT and CI4R, RadMamba achieves the best accuracy in models shown in Tab. IV and highlights its effectiveness in continuous HAR scenarios with the smallest

model size and #FLOP per inference.

Figure 5 (a) and (b) present confusion matrices comparing the ground truth labels with the best predictions of RadMamba, illustrating its classification accuracy and error distribution for each dataset. Figure 5 (c) shows the comparison between the classification results of RadMamba and CNN-LSTM over time. Complementing this, Figure 6 displays the averaged test loss across ten random seeds as a function of training epochs, providing insight into the model's convergence behavior and stability during training on the same datasets.

C. Ablation study of the Micro-doppler-oriented Structure

Table V presents an ablation study evaluating the impact of new architectural blocks in the RadMamba model across three datasets with varying radar settings. The study systematically assesses the effects of different projection layers, patch sizes, and down-sampling scales on model accuracy and parameter efficiency, with results averaged over seeds 0 to 5.

At the outset, the most important conclusion is that optimal performance emerges from the combined integration of all three proposed new blocks—projection layer, patch size, and down-sampling scale—rather than any single component in isolation. This is evident in the incremental improvements observed across the configurations. For instance, the baseline conventional ViM model (Row 1) achieves an accuracy of 93.5% on Dataset DIAT, 61.9% on Dataset CI4R, and 71.2% on Dataset UoG2020. In contrast, the proposed RadMamba (Row 27), which incorporates a 1D convolution layer, a patch size of $(H_{c-d}, 1)$, and a down-sampling (2, 2), achieves a

higher accuracy of 99.8% on Dataset DIAT. Similarly, on Dataset CI4R, Row 27 with a (2, 8) down-sampling scale yields significantly higher accuracy of 89.6%, and on Dataset UoG2020 with a (2, 32) scale, it reaches 88.6%. Intermediate configurations, such as Row 19 (only projection replacement), Row 7 (only patch size changing) and Row 2 (only down-sampling applied) show lower accuracies—underscoring that no single structure alone achieves the peak performance of the fully combined design in Row 27.

To provide a more detailed analysis, we discuss the three blocks—projection layer, patch size, and down-sampling scale—separately, evaluating their individual contributions to RadMamba’s performance across the datasets.

1) *Projection Replacement*: The adoption of a 1D convolutional layer as the projection mechanism consistently outperforms configurations with a single linear layer or three linear layers across nearly all settings. Comparing Rows 19–27 with Rows 10–18 and Rows 1–9, the conv1d projection replacement within the same patch size and down-sampling scale achieved average increment of mean accuracy by 0.48% over 1 linear layer, 0.40% over 3 linear layer on Dataset DIAT. On Dataset CI4R and UoG2020, the conv1d layer shows a substantial improvement of 2.99% and 3.64% over 1 linear layer, respectively.

2) *Patch Size*: The $(H_{c-d}, 1)$ configuration consistently delivers superior performance within each projection layer type. For the 1D convolutional layer, Row 25 with $(H_{c-d}, 1)$ and without down-sampling achieves 3% gain on Dataset DIAT, 22.4% gain on Dataset CI4R, 9.2% gain on Dataset UoG2020 vs. Row 19 with rectangular patch. This trend holds across other projection types, indicating that the $(H_{c-d}, 1)$ patch size effectively retains the critical spatial features for radar data processing.

3) *Down-sampling*: The results suggest that down-sampling along the patch vector dimension generally outperforms down-sampling along the dimension orthogonal to patch vector and no down-sampling. For instance, Row 27’s (2, 32) time down-sampling achieves $88.6\% \pm 1.46$, outperforming Row 26’s (8, 2) at $84.4\% \pm 2.05$ and Row 25’s (1, 1) at $84.5\% \pm 0.77$ on Dataset UoG2020. This pattern highlights the advantage of downsampling in enhancing the micro-Doppler features.

The ablation study underscores the efficacy of the proposed RadMamba design, with the highest performance achieved by integrating a 1D convolutional projection layer, a $(H_{c-d}, 1)$ patch size, and time-dimension down-sampling (Row 27).

VIII. CONCLUSION

RadMamba sets a new benchmark in RadHAR, delivering top-tier accuracy with minimal parameters and computational cost across diverse datasets. Its radar micro-Doppler-oriented design addresses domain-specific challenges, making it ideal for real-time, resource-constrained applications. Overall, RadMamba consistently outperforms previous neural network models like ResNet, Bi-LSTM, CNN-LSTM, and CNN-Bi-GRU, and competes with or exceeds advanced architectures like Vision Transformers and ActivityMamba, all while maintaining a remarkably low parameter count (ranging from 6.7k

to 71.4k) and reduced computational complexity (1.3M to 145.6M #FLOP/Inf.). These results emphasize RadMamba’s capability as a lightweight and high-performance solution for radar-based HAR across diverse radar modalities and activity recognition tasks. The micro-Doppler-oriented design, integrating channel fusion, Doppler-aligned segmentation, and convolutional projections, addresses the unique challenges of radar data, delivering high accuracy across CW and FMCW datasets, both continuous and non-continuous. Ablation studies confirm the synergy of its components, with no single element achieving comparable performance alone.

ACKNOWLEDGMENTS

This work was partially supported by the European Research Executive Agency (REA) under the Marie Skłodowska-Curie Actions (MSCA) Postdoctoral Fellowship program, Grant No. 101107534 (AIRHAR). We thank Prof. Dr. L.C.N. de Vreede and Prof. Dr. Alexander Yarovoy for their support.

REFERENCES

- [1] X. Li, Y. He, and X. Jing, “A survey of deep learning-based human activity recognition in radar,” *Remote Sensing*, vol. 11, no. 9, 2019. [Online]. Available: <https://www.mdpi.com/2072-4292/11/9/1068>
- [2] I. Ullmann, R. G. Guendel, N. C. Kruse, F. Fioranelli, and A. Yarovoy, “A survey on radar-based continuous human activity recognition,” *IEEE Journal of Microwaves*, vol. 3, no. 3, pp. 938–950, 2023.
- [3] Y. Kim and H. Ling, “Human activity classification based on micro-doppler signatures using a support vector machine,” *IEEE Transactions on Geoscience and Remote Sensing*, vol. 47, no. 5, pp. 1328–1337, 2009.
- [4] M. Zenaldin and R. M. Narayanan, “Radar micro-Doppler based human activity classification for indoor and outdoor environments,” in *Radar Sensor Technology XX*, K. I. Ranney and A. Doerry, Eds., vol. 9829, International Society for Optics and Photonics. SPIE, 2016, p. 98291B. [Online]. Available: <https://doi.org/10.1117/12.2228397>
- [5] B. Erol, M. Francisco, A. Ravisankar, and M. Amin, “Realization of radar-based fall detection using spectrograms,” in *Compressive Sensing VII: From Diverse Modalities to Big Data Analytics*, F. Ahmad, Ed., vol. 10658, International Society for Optics and Photonics. SPIE, 2018, p. 106580B. [Online]. Available: <https://doi.org/10.1117/12.2309817>
- [6] H. Li, A. Shrestha, H. Heidari, J. L. Kerne, and F. Fioranelli, “Activities recognition and fall detection in continuous data streams using radar sensor,” in *2019 IEEE MTT-S International Microwave Biomedical Conference (IMBioC)*, vol. 1, 2019, pp. 1–4.
- [7] H. Li, A. Shrestha, H. Heidari, J. Le Kerne, and F. Fioranelli, “Bi-lstm network for multimodal continuous human activity recognition and fall detection,” *IEEE Sensors Journal*, vol. 20, no. 3, pp. 1191–1201, 2020.
- [8] R. G. Guendel, F. Fioranelli, and A. Yarovoy, “Distributed radar fusion and recurrent networks for classification of continuous human activities,” *IET Radar, Sonar & Navigation*, vol. 16, no. 7, pp. 1144–1161, 2022. [Online]. Available: <https://ietresearch.onlinelibrary.wiley.com/doi/abs/10.1049/rsn2.12249>
- [9] Y. Kim and T. Moon, “Human detection and activity classification based on micro-doppler signatures using deep convolutional neural networks,” *IEEE Geoscience and Remote Sensing Letters*, vol. 13, no. 1, pp. 8–12, 2016.
- [10] C. Yu, Z. Xu, K. Yan, Y.-R. Chien, S.-H. Fang, and H.-C. Wu, “Noninvasive human activity recognition using millimeter-wave radar,” *IEEE Systems Journal*, vol. 16, no. 2, pp. 3036–3047, 2022.
- [11] L. Werthen-Brabants, G. Bhavanasi, I. Couckuyt, T. Dhaene, and D. Deschrijver, “Quantifying uncertainty in real time with split birnn for radar human activity recognition,” in *2022 19th European Radar Conference (EuRAD)*, 2022, pp. 173–176.
- [12] E. Kurtoglu, A. C. Gurbuz, E. A. Malaia, D. Griffin, C. Crawford, and S. Z. Gurbuz, “Asl trigger recognition in mixed activity/signing sequences for rf sensor-based user interfaces,” *IEEE Transactions on Human-Machine Systems*, vol. 52, no. 4, pp. 699–712, 2022.
- [13] J. Zhu, H. Chen, and W. Ye, “A hybrid cnn-lstm network for the classification of human activities based on micro-doppler radar,” *IEEE Access*, vol. 8, pp. 24 713–24 720, 2020.

- [14] S. Zhu, R. G. Guendel, A. Yarovsky, and F. Fioranelli, "Continuous human activity recognition with distributed radar sensor networks and cnn-rnn architectures," *IEEE Transactions on Geoscience and Remote Sensing*, vol. 60, pp. 1–15, 2022.
- [15] L. Zhu, B. Liao, Q. Zhang, X. Wang, W. Liu, and X. Wang, "Vision mamba: Efficient visual representation learning with bidirectional state space model," 2024. [Online]. Available: <https://arxiv.org/abs/2401.09417>
- [16] M. Ding, G. Dongye, P. Lv, and Y. Ding, "Fml-vit: A lightweight vision transformer algorithm for human activity recognition using fmcw radar," *IEEE Sensors Journal*, vol. 24, no. 22, pp. 38 518–38 526, 2024.
- [17] Y. Zhao, R. G. Guendel, A. Yarovsky, and F. Fioranelli, "Distributed radar-based human activity recognition using vision transformer and cnns," in *2021 18th European Radar Conference (EuRAD)*, 2022, pp. 301–304.
- [18] A. Dosovitskiy, L. Beyer, A. Kolesnikov, D. Weissenborn, X. Zhai, T. Unterthiner, M. Dehghani, M. Minderer, G. Heigold, S. Gelly, J. Uszkoreit, and N. Houlsby, "An image is worth 16x16 words: Transformers for image recognition at scale," in *International Conference on Learning Representations*, 2021. [Online]. Available: <https://openreview.net/forum?id=YicbFdNTTy>
- [19] F. Luo, A. Li, B. Jiang, S. Khan, K. Wu, and L. Wang, "Activitymamba: a cnn-mamba hybrid neural network for efficient human activity recognition," *IEEE Transactions on Mobile Computing*, pp. 1–15, 2025.
- [20] H. Ren, Y. Zhou, J. Zhu, X. Lin, H. Fu, Y. Huang, Y. Fang, F. Ma, H. Yu, and B. Cheng, "Rethinking efficient and effective point-based networks for event camera classification and regression," *IEEE Transactions on Pattern Analysis and Machine Intelligence*, pp. 1–14, 2025.
- [21] H. Sha, W. Zhaoyue, W. Xiaoqiang, W. Limei, Y. Xiaoxuan, H. Hongming, and D. Gan E, "A lightweight hybrid vision transformer network for radar-based human activity recognition," in *Sci Rep* 13, 2023, p. 17996.
- [22] M. Linardakis, I. Varlamis, and G. T. Papadopoulos, "Survey on hand gesture recognition from visual input," 2025. [Online]. Available: <https://arxiv.org/abs/2501.11992>
- [23] C. Ding, H. Hong, Y. Zou, H. Chu, X. Zhu, F. Fioranelli, J. Le Kernec, and C. Li, "Continuous human motion recognition with a dynamic range-doppler trajectory method based on fmcw radar," *IEEE Transactions on Geoscience and Remote Sensing*, vol. 57, no. 9, pp. 6821–6831, 2019.
- [24] S.-w. Kang, M.-h. Jang, and S. Lee, "Identification of human motion using radar sensor in an indoor environment," *Sensors*, vol. 21, no. 7, 2021. [Online]. Available: <https://www.mdpi.com/1424-8220/21/7/2305>
- [25] S. Hochreiter and J. Schmidhuber, "Long short-term memory," *Neural Computation*, vol. 9, no. 8, pp. 1735–1780, 1997.
- [26] J. Chung, C. Gulcehre, K. Cho, and Y. Bengio, "Empirical evaluation of gated recurrent neural networks on sequence modeling," 2014. [Online]. Available: <https://arxiv.org/abs/1412.3555>
- [27] A. Shrestha, H. Li, J. Le Kernec, and F. Fioranelli, "Continuous human activity classification from fmcw radar with bi-lstm networks," *IEEE Sensors Journal*, vol. 20, no. 22, pp. 13 607–13 619, 2020.
- [28] Wikipedia contributors, "American sign language," https://en.wikipedia.org/wiki/American_Sign_Language, 2025, accessed on April 6, 2025.
- [29] L. Tang, Y. Jia, Y. Qian, S. Yi, and P. Yuan, "Human activity recognition based on mixed cnn with radar multi-spectrogram," *IEEE Sensors Journal*, vol. 21, no. 22, pp. 25 950–25 962, 2021.
- [30] M. Chakraborty, H. C. Kumawat, S. V. Dhavale, and A. B. Raj A., "Diat-radarnet: A lightweight dcnn for radar based classification of human suspicious activities," *IEEE Transactions on Instrumentation and Measurement*, vol. 71, pp. 1–10, 2022.
- [31] S. Z. Gurbuz, M. M. Rahman, E. Kurtoglu, T. Macks, and F. Fioranelli, "Cross-frequency training with adversarial learning for radar micro-Doppler signature classification (Rising Researcher)," in *Radar Sensor Technology XXIV*, K. I. Ranney and A. M. Raynal, Eds., vol. 11408, International Society for Optics and Photonics. SPIE, 2020, p. 114080A. [Online]. Available: <https://doi.org/10.1117/12.2559155>
- [32] J. Ho, A. Jain, and P. Abbeel, "Denoising diffusion probabilistic models," 2020. [Online]. Available: <https://arxiv.org/abs/2006.11239>
- [33] D. P. Kingma and J. Ba, "Adam: A method for stochastic optimization," *arXiv preprint arXiv:1412.6980*, 2014.
- [34] I. Loshchilov and F. Hutter, "Decoupled weight decay regularization," in *International Conference on Learning Representations*, 2019. [Online]. Available: <https://openreview.net/forum?id=Bkg6RiCqY7>
- [35] K. He, X. Zhang, S. Ren, and J. Sun, "Deep residual learning for image recognition," 2015. [Online]. Available: <https://arxiv.org/abs/1512.03385>
- [36] M. Horowitz, "1.1 computing's energy problem (and what we can do about it)," in *2014 IEEE international solid-state circuits conference digest of technical papers (ISSCC)*. IEEE, 2014, pp. 10–14.